Check for updates



www.chemcatchem.org

# CO<sub>2</sub>-Hydrogenation to Methanol over CuO/ZnO Based Infiltration Composite Catalyst Spheres

Carl Fritsch,\*<sup>[a]</sup> Jürgen Dornseiffer,<sup>[b]</sup> Jule Blankenstein,<sup>[a]</sup> Michael Noyong,<sup>[c]</sup> Christian Groteklaes,<sup>[a]</sup> and Ulrich Simon<sup>[c]</sup>

Multiple active component catalysts for efficient conversion of CO $_2$  to Methanol (MeOH) are synthesized through coating  $\gamma\textsuperscript{-}Al_2O_3$  carrier spheres by incipient wetness impregnation method (IWI). The well-known bimetallic Copper Oxide/Zinc Oxide (CuO/ZnO)is promoted in three steps, first by Cerium Oxide (CeO $_2$ ), then additionally with Zirconium Oxide (ZrO $_2$ ) and finally with Calcium Oxide (CaO) resulting in four carrier catalysts with high surface area and catalyst pore volume. Quaternary and quinary carrier catalysts promoted with moderate CeO $_2$ , ZrO $_2$  in the quaternary (20% CZCZ) and additionally with CaO (20% CZCZC) in the quinary catalysts demonstrate high CO $_2$ -conversion ratios (16.2% and 18.7%) and space time yields (0.51

and 0.47  $g_{MeOH}h^{-1}g_{Catalyst}^{-1}$ ) at 5 MPa and 250 °C. The high conversion ratios ( $X_{CO2}$ ) and good methanol space-time-yields (STY<sub>MeOH</sub>) are attributed to enhanced copper dispersion and several multi metal oxide component interactions essential to enhance  $CO_2$ -activation and -conversion through the catalytic systems as well as very high overall surface area. Compared to related studies, the carrier catalysts show superior conversion rates, proving the effectiveness of the introduced multi-component carrier catalyst and extending the understanding of infiltrate composites as possible large-scale application alternatives to precipitated MeOH catalyst systems.

## Introduction

It is widely accepted that CO<sub>2</sub> concentration in the earth's atmosphere is a primary driving factor for anthropogenic climate change. To mitigate possible effects of CO<sub>2</sub> emissions into the atmosphere, CO<sub>2</sub> capture and utilization (CCU) has gained attention in research and first larger scale applications have been established in the past years. Furthermore, the recovery of CO<sub>2</sub> from regenerative sources such as biogas, sewage gas, thermal biomass treatment or from bio waste treatment processes, promises to open possibilities for substitution of fossil carbon products through biogenic alternatives.

Methanol (MeOH) is one of the most commonly used petrochemical products and base chemicals. Commercially, it is

- [a] C. Fritsch, J. Blankenstein, C. Groteklaes Environmental and Process Engineering (UVT), Research Institute for Water Management and Climate Future at RWTH Aachen University (FiW), Kackertstraße 15–17, 52072 Aachen, Germany E-mail: fritsch@fiw.rwth-aachen.de
- [b] J. Dornseiffer Institute of Energy and Climate Research: Materials Synthesis and Processing (IEK-1), Forschungszentrum Jülich GmbH, Wilhelm-Johnen-Straße, 52428 Jülich, Germany
- [c] M. Noyong, U. Simon Institute of Inorganic Chemistry (IAC), RWTH Aachen University, Landoltweg 1a, 52074 Aachen, Germany
- Supporting information for this article is available on the WWW under https://doi.org/10.1002/cctc.202400731
- © 2024 The Authors. ChemCatChem published by Wiley-VCH GmbH. This is an open access article under the terms of the Creative Commons Attribution Non-Commercial NoDerivs License, which permits use and distribution in any medium, provided the original work is properly cited, the use is non-commercial and no modifications or adaptations are made.

produced from natural gas through a multistage process comprising of synthesis gas production by steam reforming of the feed gas and subsequent catalytical generation of MeOH of the carbon monoxide-rich gas. Alternatively, MeOH can be produced directly through hydrogenation of  $\rm CO_2$ . Catalyst development to increase activity and selectivity of known catalyst complexes towards MeOH in the hydrogenation of  $\rm CO_2$  has thus attracted great interest in the past years.

Industrial MeOH catalysts are mostly based upon ternary metal oxide mixtures, with CuO being the main active component. ZnO and  $Al_2O_3$  are widely regarded as the most efficient additional components for CO-conversion to MeOH and are thus used in most commercial fossil MeOH applications. [2-5]

As the ternary commercial catalysts show low activity, mediocre selectivity towards MeOH in CO<sub>2</sub>-hydrogenation and limited long-term stability, a wide range of possible metal oxide promoters and catalyst supports for more efficient conversion have been tested in recent studies.<sup>[6-8]</sup> Herein, some key factors for improved CO<sub>2</sub>-adsorption and -conversion have been identified: good Cu species dispersion, creation of large boundary metal interfaces and provision of oxygen vacancies are some of the most prominent, with certain metal promoters being able to induce all of the described promotional effects. Among others, CeO<sub>2</sub> has been shown to provide essential active sites for CO<sub>2</sub>-adsorption, providing both active Cu-metal interfaces and creating oxygen surface vacancies, both of which have been proven to improve CO<sub>2</sub>-conversion in CuO-ZnO catalyst. [9-12] Furthermore, CeO<sub>2</sub> has advanced redox ability, is very stable and exhibits inverse valence transformation ( $Ce^{4+} \rightarrow$ Ce<sup>3+</sup>) thus providing an acting point for oxygen-containing bonds.[13] ZrO<sub>2</sub> has been in the focus of methanol catalyst development for some years now. It has been proven to



substantially increase Cu-species dispersion and provide further vacancies for improved adsorption. [14-21] Furthermore alkaline and alkaline earth metals such as K or Mg have been shown to strongly promote dispersion in Cu-based methanol catalysts and provide surface alkalinity, which has been shown to improve CO<sub>2</sub> activation capacity. [22-26] Many studies have also investigated the reciprocal effects of the combination of several catalyst metal oxides and catalyst supports, with emphasis on the unique synergistic effects of CuO and ZnO for hydrogenation of CO and CO<sub>2</sub>. [27-31] But examination of synergistic effects for several active components in CuO-based ternary, quaternary or quinary catalyst structures have shown promising results in enhancing MeOH selectivity, improving catalyst long term stability and increasing conversion ratios. Zablinksy et al. (2021) reported, that CeO<sub>2</sub>/ZrO<sub>2</sub> interplay on ternary catalysts played a vital role in conversion efficiency and MeOH selectivity. [32] Poto et al. (2022) showed, that CuO/ZrO<sub>2</sub>/CeO<sub>2</sub> catalysts were highly efficient for hydrogenation of CO2 and ZrO<sub>2</sub>/CeO<sub>2</sub> interplay was able to increase selectivity for methanol compared to commercial CuO/ZnO/Al<sub>2</sub>O<sub>3</sub> catalysts.<sup>[33]</sup> Further positive synergistic effects in ternary and quaternary catalyst structures containing ZrO<sub>2</sub>, CeO<sub>2</sub> or both for CO<sub>2</sub>hydrogenation have also been reported in studies published recently.[34-37]

Most industrial catalysts and many studied catalyst in research are produced by co-precipitation of the catalytically active metal oxides.  $^{[2,4,24]}$ 

In recent years, various approaches for catalyst production have been discussed for simplified catalyst sample manufacturing based around impregnation techniques for carrier catalysts. Samples produced by the IWI method promise an increase in catalyst surface area and sufficient dispersion of catalytically active components on the catalyst surface, while reducing catalyst production cost and technical complexity in catalyst manufacturing. While Al<sub>2</sub>O<sub>3</sub> has long been a prominent carrier material, different approaches for its use have been reported in recent studies: Bansode et al. (2013)<sup>[22]</sup> introduced γ-Al<sub>2</sub>O<sub>3</sub> spheres as carrier for the catalyst, while testing alkaline earth metal oxide promoters for enhanced CO<sub>2</sub>-conversion and Ren et al. (2015)<sup>[24]</sup> extended upon their work. Both studies showed promising results, concluding that  $\gamma$ -Al<sub>2</sub>O<sub>3</sub> is a suitable carrier for catalytically active multi metal oxide combinations and tested carrier catalysts were able to deliver high conversion ratios and good MeOH selectivity. This plays a vital role in formulating high performance catalyst compositions for future commercial applications of CO<sub>2</sub>-to-MeOH.

In the herein presented work, findings from aforementioned studies are combined in an attempt to extend upon existing work and further deepen the understanding for catalyst performance in CuO/ZnO based ternary, quaternary and quinary catalyst structures. To investigate the effects of CeO<sub>2</sub> and ZrO<sub>2</sub> promotion of binary CuO/ZnO catalyst and to further study the effects of earth alkaline catalyst promotion such as CaO, four carrier catalysts for efficient hydrogenation of CO<sub>2</sub> to MeOH are prepared as infiltration composites by IWI. Highly porous alumina support spheres are coated with 20 wt% of the different catalyst metal oxide compounds. The resulting catalyst

samples are tested for activity and selectivity towards  $CO_2$ -hydrogenation to MeOH.  $\gamma$ -Al $_2O_3$  spheres were used as catalyst support to guarantee a uniform and comparable catalyst bed for each sample during activity measurements.

To highlight synergistic effects for multiple active catalyst materials, a base catalyst CuO-ZnO on alumina was used for further incremental promotion of the proven binary catalytic system. While maintaining molar ratios for CuO and ZnO we added CeO<sub>2</sub>, ZrO<sub>2</sub> and CaO in promotional steps, thus preparing four different catalyst samples for physio-chemical characterization and catalyst screening towards performance of CO<sub>2</sub>-hydrogention to methanol. For comparison a commercial CuO/ZnO/Al<sub>2</sub>O<sub>3</sub> catalyst containing 63.5 wt% CuO, 25.0 wt% ZnO, 10.0 wt% Al<sub>2</sub>O<sub>3</sub> and 1.5 wt% MgO was also tested as a reference.

All catalyst samples were subjected to different physiochemical analyses. Brunauer-Emmett-Teller (BET), surface area and pore size distribution were determined. For analysis of surface topography and elemental distribution on the catalyst surface, scanning electron microscopy (SEM) with integrated energy dispersive X-ray spectroscopy (EDX) was applied. X-Ray diffraction (XRD) was used for determination of the phase composition. Surface acidity was determined by ammonia temperature programmed desorption (NH<sub>3</sub>-TPD), while reducibility was probed by hydrogen temperature programmed reduction (H<sub>2</sub>-TPR).

# **Results and Discussion**

# **Results Sample Characterization**

For better understanding of the possible catalytic interface involved in  $CO_2$ -hydrogenation, analyses of specific BET surface areas, pore size distribution and pore volume were carried out for all samples (Abbreviation protocol and manufacturing protocols for all herein tested samples are described in experimental section). Calculated catalytic surface areas ( $A_{\text{BET}}$ ), total average pore volume ( $V_{\text{TOT}}$ ) and average pore diameter ( $D_{\text{Pore}}$ ) of the coated catalysts, the uncoated  $Al_2O_3$  carrier spheres and a crushed and sieved reference catalyst sample are listed in Table 1. The uncoated alumina spheres exhibit the highest

**Table 1.** Specific surface areas  $(A_{BET})$  and corresponding pore volumes of the catalysts in comparison to the supporting  $Al_2O_3$  spheres and the reference.

Sample	${\sf A}_{\sf BET} \ {\sf m}^2 \!\cdot\! {\sf g}^{-1}$	$V_{TOT}$ $cm^3 \cdot g^{-1}$	D <sub>Pore</sub> nm				
Reference	76	0.18	8.85				
γ-Al <sub>2</sub> O <sub>3</sub>	151	0.48	-				
20 % CZ <sup>[a]</sup>	132	0.36	10.71				
20 % CZC <sup>[a]</sup>	122	0.34	11.30				
20 % CZCZ <sup>[a]</sup>	129	0.37	11.37				
20% CZCZC <sup>[a]</sup>	125	0.36	11.55				
[ ] 200/							

[a] 20 %w catalyst coating on 800 μm carrier spheres.

specific surface area and the highest specific pore volume in this comparison. Through catalyst coating, overall  $A_{BET}$  and  $V_{TOT}$  are consistently reduced through the different stages of catalyst promotion, although the measured surface areas of presented catalyst samples stay inside a range of 10%, overall surface area deviation is therefore limited. Compared to uncoated  $Al_2O_3$ ,  $A_{BET}$  of 20% CZCZC is reduced by 17% and  $D_{Pore}$  by 25%.

All coated catalysts exhibit intercomparable average pore diameters derived from BET measurements. Compared to the industrial pellet catalyst, catalytic boundary area is increased by up to 65% and total average pore volume by up to 100%. For better understanding of the presented measurements, adsorption isotherms for the carrier and each catalyst are given in the supplementary materials (Figure S1–S6).

To determine the phase composition on the sample surfaces, the catalysts were analyzed by powder X-ray diffraction according to the protocol described in the experimental section. Figure 1 exhibits the resulting diffractograms of the infiltration composite in comparison to the reference and the alumina spheres used as support material. In general, the catalysts exhibit a comparable typical nanocrystalline diffraction pattern with very broad wave-like peaks.

The few pronounced peaks from the  $2\Theta$  positions at  $35.5^\circ$ ,  $38.7^\circ$  and  $48.7^\circ$  for the pure CuO/ZnO catalyst (20 % CZ) can be assigned to CuO with a monoclinic structure, which become smaller and broader in intensity with increasing promoter doping.

This indicates a decreasing CuO particle size and thus a higher specific catalytic interface in the same direction. An average crystallize size of the copper oxide in the 20% CZ catalyst was determined to be 30 to 40 nm using the Scherrer formula on the full width at half maximum (FWHM) of the main peak at  $2\Theta\!=\!35.5^\circ$ , whereas a CuO particle size of approx. 12 nm is determind for the industrial reference catalyst. ZnO as

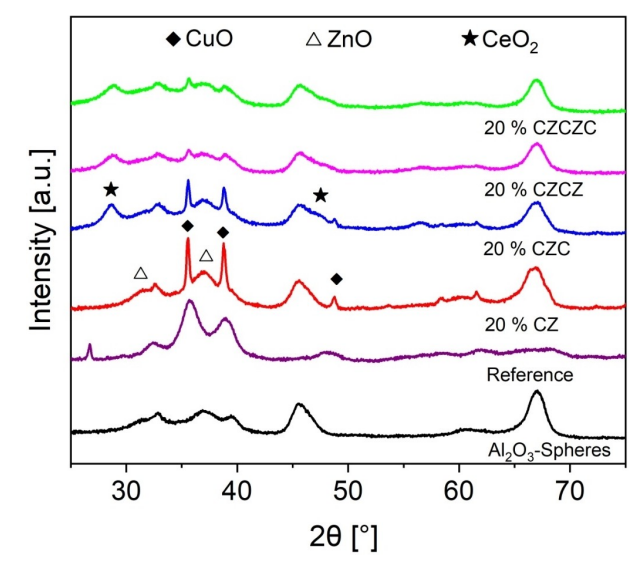


Figure 1. Powder X-ray diffraction patterns of the different catalysts in comparison to the reference and the used alumina spheres. The diamond icon is used for identification of distinctive Cu-diffraction peaks, while star and triangle identify  $CeO_2$  and ZnO respectively.

the second main component of all herein presented catalyst samples can be identified via the broad peaks at  $2\Theta=32.5^\circ$  and  $2\Theta=36.3^\circ$ , which are, however, superimposed by the  $\gamma\text{-Al}_2O_3$  of the support material. Furthermore, the broad diffraction peak at  $2\Theta=28.6^\circ$  could be assigned to  $\text{CeO}_2$  in the catalysts containing cerium. The crystalline phase of the ZrO $_2$  in the 20% CZCZ and 20% CZCZC catalysts and the Al $_2O_3$  in the industrial catalyst could not be detected. Solely the peak at  $2\Theta=26.6^\circ$  of the reference could be identified as graphite (JCPDS 26-1079), which is added to the catalyst powder as an additive for molding during the extrusion process.

Another significant aspect of physical catalyst properties is the morphology of the catalyst surface and the elemental distribution within the multi-metal-oxides on the catalyst surfaces. Figure 2 shows the SEM images of all catalyst samples whereas Figure 3 reveals the corresponding element mappings of the observed area by EDX analysis.

For each catalyst sample, two images and mapping overlays are shown for demonstration of the heterogenous character of the produced carrier catalysts with areas where the multi-metal oxides are located and catalyst regions dominated more by Al<sub>2</sub>O<sub>3</sub>-carrier surface material As can be deducted from Figure 2, the surface morphology of the coated catalyst samples changes through increasing level of promotion from more coarsely grained, flake shaped particles to structures based on very small flake particles. The reference catalyst shows an even, homogeneous distribution of small particles, except for comparatively large bulk carbon structures, as can be clearly seen in the maps shown Figure 3, where elemental carbon is marked in red color for the dispersion maps from EDX analyses. This adds to the XRD findings, confirming the presence of graphite particles in the commercial catalyst, presumably stemming from manufacturing. The images of all carrier catalysts show homogenous portions with macro porous rough crystallite particles formed in bulbous formations on the surface. The structural manifestation of the formations changes with increasing catalyst promotion, which is attributed to the change in metal oxide structure with the addition of ZrO<sub>2</sub> to the catalyst surface. EDX analysis of the shown images confirm very sufficient Cu and Zn dispersion around the porous catalyst structures. Overall, the surface distribution of metal oxides proposed in the production protocol for the carrier catalyst (see materials section for production protocol), is confirmed by EDX analyses of the image sections depicted in Figure 2. Additional single element mappings further validate the even dispersion of metal oxide additives on the carrier surfaces (Supplementary materials Figures S17-S26).

Graphs and distribution tables for elemental analysis of the image sections are given as supplementary materials in Figures S7–S16 and Tables S1–S10). Overall ZrO<sub>2</sub>, CeO<sub>2</sub> and CaO loading is close to the calculated theoretical composistion and elemental distribution is hereby confirmed. While multi-metal-oxide formation with CuO, CeO<sub>2</sub> and ZrO<sub>2</sub> in the coating process can be an issue for metal dispersion on the catalyst surface, this cannot be confirmed based upon the EDX images shown in Figure 3.<sup>[38]</sup> Especially the images for 20% CZCZC show very even distribution of ZrO<sub>2</sub> and CeO<sub>2</sub> particles on the catalyst

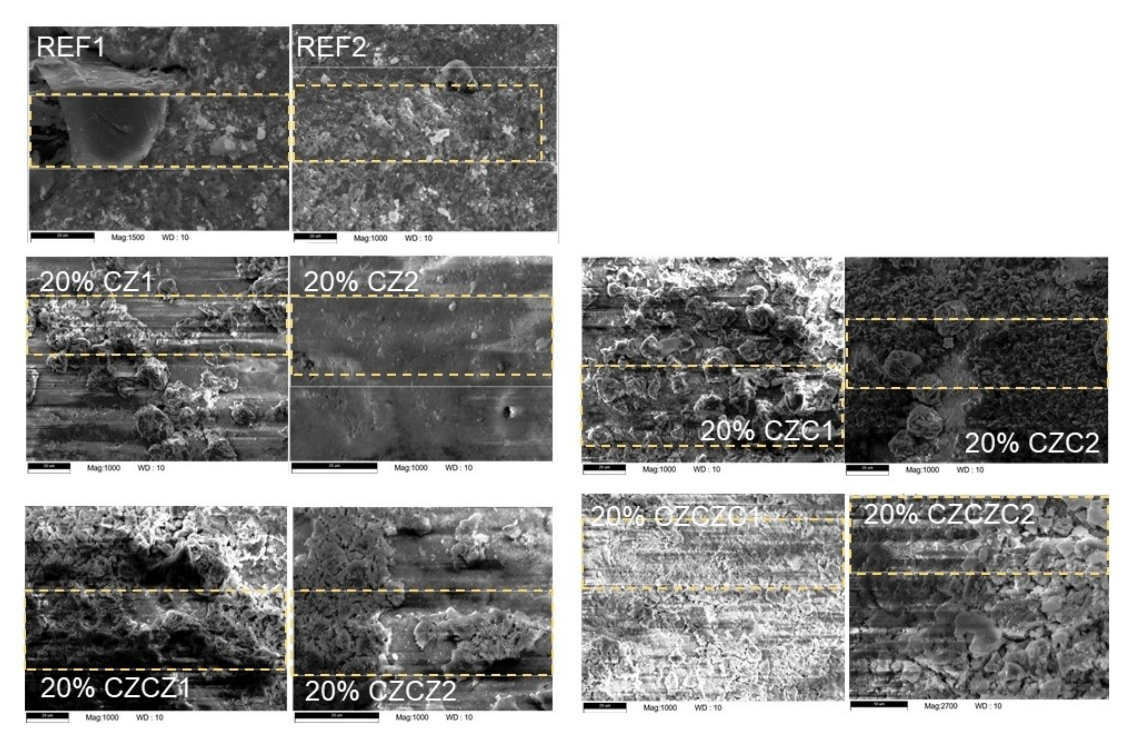


Figure 2. Highly magnified SEM images of the catalyst surfaces. Two SEM images for each catalyst sample are used, to demonstrate the inhomogeneous catalyst structures, both in the reference and in the carrier catalysts. Image sections used for EDX analyses are marked by yellow boxes. Corresponding EDX mappings are presented in Figure 3.

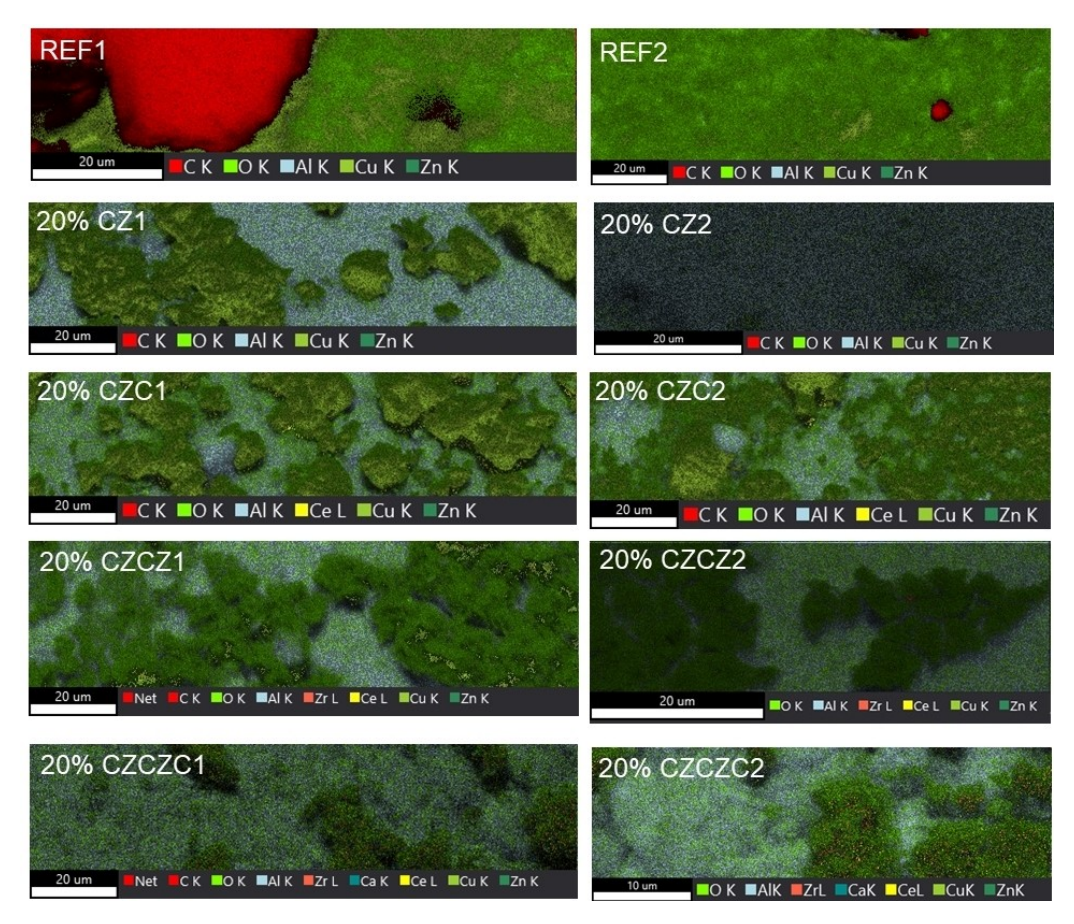


Figure 3. EDX mapping overlays for all metal components in the herein presented catalyst samples. Each mapping corresponds to an image section presented in Figure 2.

surface, indicating small particle sizes and good overall dispersion in the catalyst coating.

TPR tests were conducted for all catalyst samples and the reference catalyst for determination of  $H_2$ -reducibility and investigation of possible catalyst activity. Figure 4 shows TCD signal intensity for the measurements conducted for the TPR reactor outlet gases of the tested samples.

All samples except for 20% CZ exhibit three overlapping reduction peaks for  $H_2$ -consumption. Onset reduction temperature is around  $98\,^{\circ}\text{C}$  for the reference catalyst. The samples tested for this present work exhibit prolonged reduction onset with  $H_2$ -consumption starting at around  $150\,^{\circ}\text{C}$  for the carrier catalyst samples. For the reference, the first minor reduction peak follows at around  $210\,^{\circ}\text{C}$  ( $\alpha$ ) This primary reduction peak is found in 20% CZC, 20% CZCZ and 20% CZCZC as well, but is clearly most pronounced in the reference catalyst.

This weakly pronounced primary peak is strongly integrated with the more strongly pronounced second peak at around 225 °C ( $\beta$ ) and a shoulder peak at around 265 °C ( $\gamma$ ) for the reference catalyst. Calculated peak positions are given in Table 2. As only CeO<sub>2</sub>, CuO and ZnO can be reduced in the

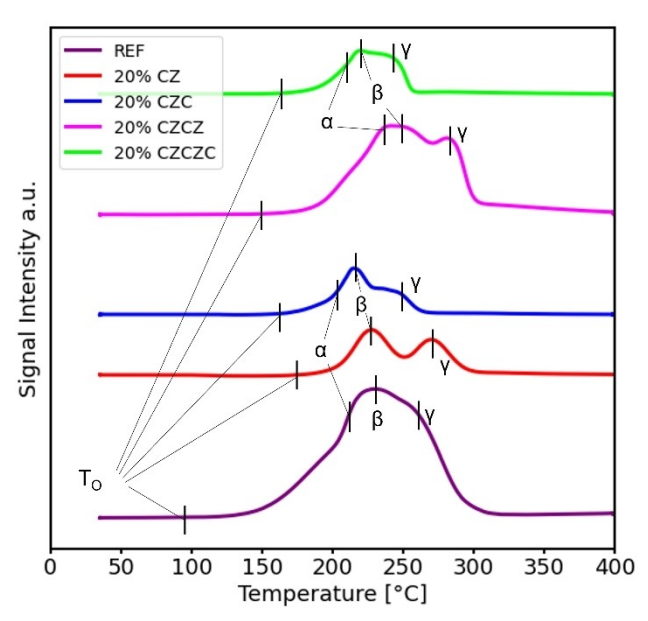


**Figure 4.** H<sub>2</sub>-TPR profiles of the catalysts compare to the industrial reference. T<sub>O</sub> marks onset reduction temperature. α, β and γ are used for marking the three distinctive reduction peaks. T<sub>O</sub> – Onset reduction for first reduced, small and widely dispersed CuO particles; α – Onset reduction peak at around 190–220 °C; β – Main reduction peak at around 200–225 °C; γ – Shoulder peak at around 240–280 °C caused by more strongly interacted CuO species.

measured temperature range, reduction peaks can mostly be attributed to reduction of different CuO species or interacted CuO.<sup>[11,39]</sup>

 $\alpha$  can be associated with CuO bulk reduction of isolated CuO species or composite metal oxides, while higher reduction temperatures can be attributed to CuO that are strongly interacted with other metal oxide species, thus inducing hard reducibility of  $\text{Cu}^{2+}$  species.  $^{[11]}$ 

It is noteworthy, that the reference catalyst shows the lowest reduction temperatures of all tested samples, although not by substantial margins. This indicates CuO being less strongly interacted and generally more evenly dispersed by particle size, which is expected in precipitated solid catalyst.

As the degree of catalyst promotion through CeO $_2$ , ZrO $_2$  and CaO increases from 20% CZ to 20% CZCZC, both  $\beta$  and  $\gamma$  decrease in height and width substantially.

This indicates both bulk CuO and well dispersed, weakly interacted Cu species decrease in prevalence and catalyst surface distribution. 20% CZC catalyst structure exhibits the lowest reducibility with CeO<sub>2</sub> addition not improving reducibility of the catalyst sample over 20% CZ. The addition of ZrO<sub>2</sub> in 20% CZCZ greatly increases overall reduction properties over 20% CZC and 20% CZ, with reduction onset temperature being lowered and all overlapping reduction peaks increasing in height and width. 20% CZCZ exhibits the highest specific H<sub>2</sub>-consumption in all carrier catalyst with a total H<sub>2</sub>-consumption of 0.038  $g_{\rm H2}/g_{\rm active}$  cat component referring to the 20% active component in the compound catalyst. Especially the first reduction peak  $\alpha$  is increased in surface area, which indicates  ${\rm ZrO_2}$  ability to disperse other metal oxide species on the carrier surface and produce more evenly distributed metal oxide pores.

ZrO $_2$  seems to additionally increase reducibility of CuO and CeO $_2$  with overall H $_2$ -consumption increased threefold over 20% CZC. Addition of CaO decreases overall reducibility over 20% CZCZ. This is attributed to the metal oxide species being interacted in more complex manners than in the ternary and quaternary catalyst samples 20% CZC and 20% CZCZ. Overall, the complex interactions lead to reduction temperatures for both  $\alpha$  and  $\beta$  being raised slightly for increasing catalyst promotion, which indicates both CuO species being interacted in more complex metal oxide compound structures, making them harder to reduce inside the tested temperature window.

CO<sub>2</sub>-hydrogenation to methanol often depends on catalyst basic sites for CO<sub>2</sub>-adsoprtion on the catalyst surface. At the same time, it has been reported, that catalyst acid sites stemming from different alumina species can lead to formation

<b>Table 2.</b> Onset catalyst reduction temperature ( $T_0$ ) and temperature peaks for the three distinctive reduction peaks for each catalyst ( $\alpha$ , $\beta$ , $\gamma$ ).						
Catalyst	T <sub>o</sub> [°C]	α [°C]	β [°C]	γ [°C]	$H_2$ consumption [g/g <sub>active cat mass</sub> ]	
Reference	98	219	232	261	0.0649	
20 % CZ	176	-	226	272	0.0150	
20 % CZC	160	206	217	248	0.0129	
20 % CZCZ	140	239	254	283	0.0380	
20 % CZCZC	163	218	219	242	0.0125	

of  $C_{2+}$  molecules from synthesis gas or from methanol itself, as applied in methanol conversion to other chemicals. [27] Furthermore, earth alkali modified methanol catalysts often present good options for the synthesis of higher alcohols or the reduction of surface acid cites in catalysts, thus the addition of CaO to the promoted catalysts in this work. [40,41] To investigate the acidity of the tested catalysts, NH<sub>3</sub>-TPD analyses were carried out in a temperature range from 50 °C to 500 °C, results are given in Figure 5.

The tested samples all show overall low acidity, the magnitude of desorption plot is increased for better recognizability of progression over temperature. All catalysts exhibit two distinctive desorption peaks, one at low temperatures of around 120°C to 150°C and one at around 240°C to 270°C, which correspond to weak Brønsted acid sites for the lower temperatures and stronger Lewis acid sites for high temperatures. The reference catalyst shows the least pronounced peaks, indicating low acidity. Increasing promotion of the tested catalyst samples of this work leads to increased catalyst acidity, although the binary catalyst 20% CZ also exhibits increased acidity over the reference.

The increase in surface acidity can have a number of reasons. The overall baseline increase over the reference is attributed to the formation of intrinsic acidic alumina species on the catalyst carrier spheres and acidic sites at the metal oxide interfaces between carrier and coating. Additionally, both CeO<sub>2</sub> and ZrO<sub>2</sub> form highly acidic species, especially in interference with other metal oxides. This can be observed through the results of NH<sub>3</sub>-TPD, as 20% CZC and 20% CZCZ show largely increased desorption peaks, both in height and in width compared to the unpromoted 20% CZ and reference catalysts.

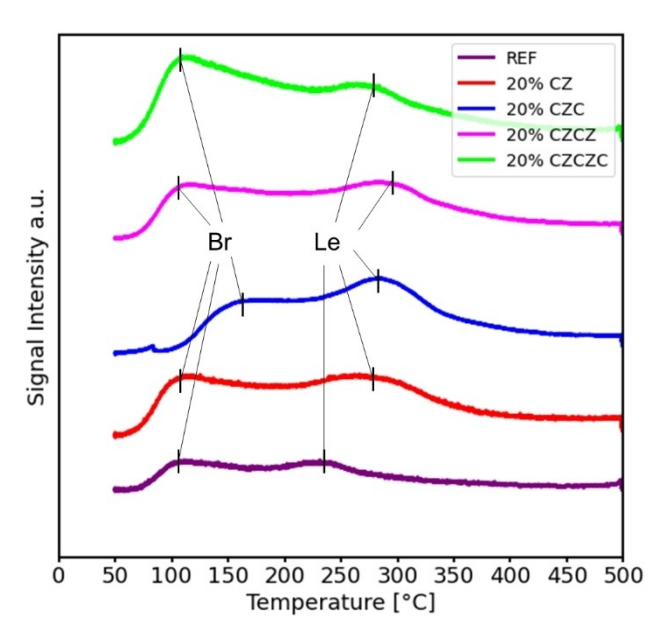


Figure 5. NH<sub>3</sub>-TPD profiles of the catalysts compare to the industrial reference. Magnitude for TCD signal is increased fivefold for better identifiability of desorption peaks. Br – Brønsted acid cites for weakly acidic surface acid components; Le – Lewis acid cites – more strongly interacted with NH<sub>3</sub> in testing.

20% CZCZC shows the steepest desorption peaks, both for Brønsted and for Lewis acid-cites. This is a contradiction to the goal of acid cite compensation through addition of CaO as metal oxide promoter. It is therebysuggested, that CaO is not effective in compensating the acidity of the alumina catalyst carrier acidity. In future work, TPD measurements for acidic gases or NMR-analyses will be added for better understanding of the acid-alkaline-interplay for the presented catalysts.

## **Catalyst Performance**

Catalyst performance was determined for different synthesis pressures, gas hourly space velocities (GHSV) and reactor temperatures using a custom laboratory catalyst test bench equipped with a 70 ml tubular reactor as shown in Figure 8 and described in further detail in the experimental section. Product gas composition was determined by an online gas chromatography unit (GC), off gas composition was determined by inline gas measurements. For typical performance testing, 35 min test protocols were conducted. Temperature, gas composition, pressure and flow rate were set and the catalyst was treated on stream for 10 min or until normalization of online temperature, pressure and off-gas composition measurements were observed. This was followed by a 20 min timed test run for determination of conversion performance. GC measurements were initiated after the 20 min steady state run.

Experiments for  $CO_2$  conversion proficiency were carried out with a constant  $H_2/CO_2$  mixture at three different gas space velocities of  $8,000\ h^{-1}$ ,  $10,000\ h^{-1}$  and  $12,000\ h^{-1}$ , three pressures of 2, 3.5 and 5 MPa and three temperatures at  $225\ ^{\circ}C$ ,  $250\ ^{\circ}C$  and  $275\ ^{\circ}C$ .  $CO_2$  to  $H_2$  ratio was set to hyper stoichiometric conditions using the stochiometric number (SN), calculated according to Equation (1) and set typically to 3:

$$SN = \frac{\dot{n}_{H_2, inlet} - \dot{n}_{CO_2, inlet}}{\dot{n}_{CO_2, inlet} + \dot{n}_{CO, inlet}}$$
(1)

Catalyst performance was evaluated through calculation of  $CO_2$ -conversion ( $X_{CO_2}$ ), product selectivity for MeOH,  $H_2O$ , CO,  $CH_4$ , DME ( $S_y$ ) and methanol production rate  $STY_{MeOH}$  rate according to following Equations (2–4):

$$X_{CO_2} = \frac{\dot{n}_{CO_2,in} - \dot{n}_{CO_2,out}}{\dot{n}_{CO_2,in}}$$
 (2)

$$S_{y} = \frac{\dot{n}_{y,out}}{\dot{n}_{MeOH,out} + \dot{n}_{CO,out} + \dot{n}_{H_{2}O,out} + \dot{n}_{CH_{4},out} + 2\dot{n}_{DME,out}}$$
(3)

$$S\dot{T}Y_{MeOH} = \frac{\dot{m}_{MeOH, out}}{m_{Catalyst}} \tag{4}$$

 $\rm X_{CO2}$  and STY $_{MeOH}$  for different reactor pressures at 250  $^{\circ}$ C reactor temperature and GHSV of 10,000-1 are shown in Figure 6.

Unsurprisingly,  $X_{CO2}$  increases significantly for all tested catalyst samples with increasing reaction pressure, where the

online library.wiley.com/doi/10.1002/cctc.202400731 by Forschungszentrum Jülich GmbH Research Center, Wiley Online Library on [15/11/2024]. See the Terms and Conditions (https://onlinelibrary.wiley.com/

-conditions) on Wiley Online Library for rules of use; OA articles are governed by the applicable Creative Comm

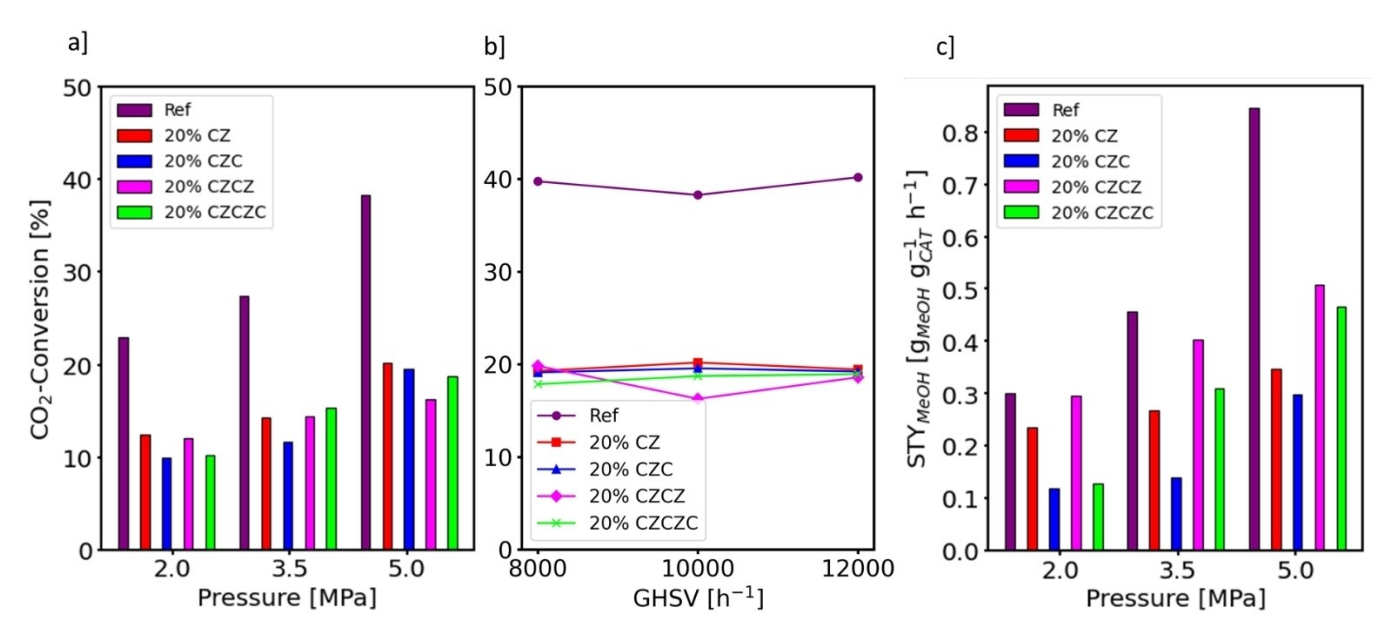


Figure 6. a)  $CO_2$ -conversion over reactor pressure for the catalyst samples at 250 °C reactor temperature, GHSV at 10,000 h<sup>-1</sup>. b)  $CO_2$ -conversion over GHSV at 250 °C reactor temperature and 5 MPa reactor pressure, c) methanol production rate over reactor pressure for the catalyst samples at 250 °C reactor temperature, GHSV at 10,000 h<sup>-1</sup> and gas composition SN = 3 for  $H_2/CO_2$ .

industrial reference exhibits the highest  $X_{CO2}$  rates and  $STY_{MeOH}$  across the presented pressure range. For the infiltration composite catalyst, increasing catalyst promotion leads to overall increases in activity concerning  $X_{CO2}$  and methanol production rate compared to the binary CuO/ZnO carrier catalysts.

X<sub>CO2</sub> for the base catalyst 20% CZ was 12% at 2 MPa and increased to 14 and 20.1% for 3.5 and 5.0 MPa respectively. This demonstrates the high effectiveness of CuO/ZnO/Al<sub>2</sub>O<sub>3</sub> catalysts in low pressure methanol synthesis. The addition of CeO<sub>2</sub> over the base CuO/ZnO catalyst initially reduces conversion and production rates for all tested pressures This result is rather unexpected, as existing literature suggests a beneficial impact for CeO<sub>2</sub> towards CO<sub>2</sub>-adsorption and hydrogenation through generation of highly active lattice oxygen and oxygen vacancies in the ternary CuO/ZnO/CeO<sub>2</sub> catalyst structure and aid in higher dispersion levels for CuO and ZnO.<sup>[47–49]</sup> Further addition of ZrO<sub>2</sub> significantly increases activity levels of the tested catalysts above the previous ternary composition and achieves conversion rates comparable or superior to the binary CuO/ZnO catalyst.

This demonstrates the importance of multiple active components in the hydrogenation of CO<sub>2</sub>. Especially the ternary interfaces between CeO<sub>2</sub>, ZrO<sub>2</sub> and CuO have been shown to produce highly active catalyst compounds. The increase in catalytic activity can be attributed to widely dispersed multi metal oxide interfaces which unite active centers for CO<sub>2</sub>-adsorption – Cu<sup>0</sup> species, oxygen vacancies and lattice oxygen in supported CeO<sub>2</sub> und ZrO<sub>2</sub> and ZnO – and H<sub>2</sub>-adsorption – widely accepted to be located in Cu and Zn catalyst surface species. [24,50,47]

CaO addition to the effective  $CuO/ZnO/CeO_2/ZrO_2$  catalyst structure further improves conversion rates at 3.5 and 5.0 MPa

slightly. The CaO promoted catalyst achieves a maximum of  $18\%~X_{CO2}$  and an hourly methanol production rate of  $0.46~g_{MeOH}~g_{Cat}^{-1}~h^{-1}$  at 5.0~MPa. Total methanol production rates for 20%~CZCZC are reduced slightly compared to 20%~CZCZ, which can be attributed to less  $CO_2$  being converted to MeOH and more being converted to byproducts of the hydrogenation, primarily CO though RWGS. This contradicts previous research, which indicates that certain levels of alkali and alkali earth catalyst promotion are able to reduce RWGS selectivity substantially.  $^{[22-24,51]}$  This also indicates, that multi-metal oxide interplay can induce inverse synthesis effects, depending on used catalyst metals and metal ratios for catalyst loading. This again is in line with previous studies, that investigated metal oxide and metal support interactions.  $^{[12,21,35,37]}$ 

Results for  $X_{CO2}$  and  $STY_{MeOH}$  for varied synthesis temperatures and for production selectivity of MeOH, CO,  $CH_4$  and DME at 3.5 MPa are given in Figure 7a) and b) respectively.

High synthesis temperatures generally lead to high conversion rates but also facilitate increased reduction of  $CO_2$  to CO and  $H_2O$  via RWGS. For all tested catalysts CO is the main carbon byproduct in  $CO_2$ -hydrogenation.

Extending on the findings from Figure 7, the reference catalyst shows the highest conversion ratios of  $CO_2$  and subsequently exhibits the highest MeOH production rates across the tested temperature range.

20% CZ and 20% CZC exhibit both the lowest conversion ratios as well as the highest selectivity values for CO<sub>2</sub>-reduction to CO. This is clearly reflected in the lowest space time yields for MeOH 0.24  $g_{\text{MeOH}}g_{\text{Cat}}^{-1}h^{-1}$  and 0.31  $g_{\text{MeOH}}g_{\text{Cat}}^{-1}h^{-1}$  respectively at 3.5 MPa and 275 °C The impregnation catalysts show overall low activity for the lower two of the tested temperatures. This indicates that catalyst activity of the composites is generally low for synthesis temperatures beneath 250 °C.

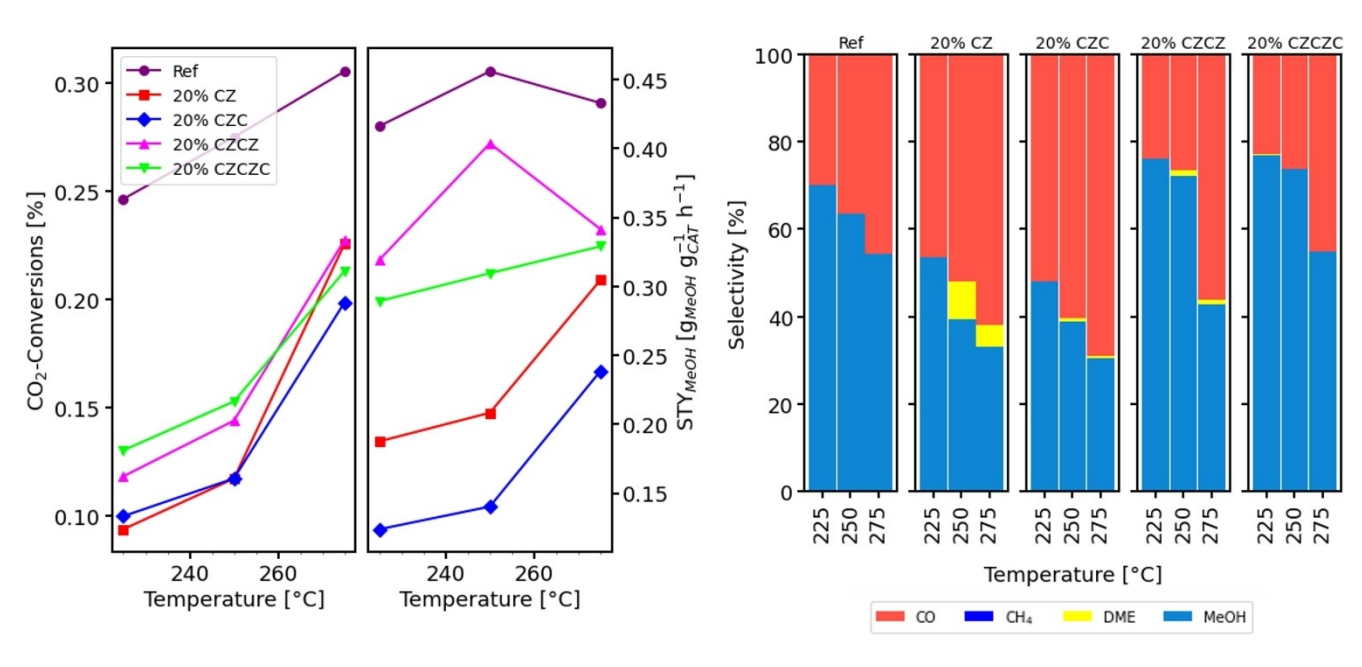


Figure 7. a) CO<sub>2</sub>-Conversion and Methanol STY for different reactor temperatures. b) Selectivity for MeOH, CO, CH<sub>4</sub> and DME generation at different temperatures. Catalyst performance was tested at 3.5 MPa reaction pressure, GHSV of  $10,000 \, h^{-1}$  and  $H_2/CO_2$  of SN = 3.

The addition of ZrO<sub>2</sub> and CaO to 20% CZC increases selectivity for MeOH and leads to an increase in production rates. As CO<sub>2</sub>-hydrogenation follows one of multiple possible pathways, this can be attributed to a number of mechanistic effects. The promotion of the ternary 20% CZC catalyst with ZrO<sub>2</sub> facilitates the hydrogenation through the formiate or carbonate pathways, which are generally associated with stable CO<sub>2</sub>-adsorption on oxygen vacancies or lattice oxygen in ZnO, CeO<sub>2</sub> and ZrO<sub>2</sub>, on the surface of Cu-species with adsorbed H<sub>2</sub> as formiate or on active interface sites between CuO and catalyst promoters or catalyst support. [10,11,22,52,53] This reaction mechanism does not contain CO as adsorbed intermediate and thus does not hazard the premature desorption of CO and H<sub>2</sub>O. Furthermore, ZrO<sub>2</sub> and CaO strongly enhance the wide dispersion of Cu-species on the carrier surface and thus facilitate wide availability of active sites for both dissociative H<sub>2</sub>and CO<sub>2</sub>-adsorption. This enables efficient reaction of adsorbed reactants and inhibits desorption of reduced CO without further interaction with topologically closely adsorbed H.

This also corresponds to the TPD and TPR results (see Figure 4 and 5), which suggest that dispersion of CuO is considerably increased by catalyst promotion through  $ZrO_2$  and CaO in 20% CZCZ and 20% CZCZC respectively.

These finding also confirm results from abovementioned studies preliminarily, suggesting positive effects of low amounts of earth alkaline catalyst promotion towards effective dispersion of CuO and ZnO and thus optimized CO<sub>2</sub>-activation for adsorption and further hydrogenation.<sup>[22]</sup>

Maximum space time yield for the infiltration composite catalysts is achieved by 20% CZCZ at 5.0 MPa, 250 °C and a GHSV for feed gas of 10.000  $h^{-1}$  at 0.507  $g_{\text{MeOH}}g_{\text{Cat}}^{-1}h^{-1}$ . 20% CZCZC achieves a maximum production rate of 0.50  $g_{\text{MeOH}}g_{\text{Cat}}^{-1}h^{-1}$  with 19,9%  $X_{\text{CO2}}$  at 5 MPa, GHSV of

12,000 h<sup>-1</sup> and 275 °C reactor temperature. For comparison, the reference catalyst achieves a maximum production rate of 1.14  $g_{MeOH}g_{Cat}^{-1}h^{-1}$  at 5.0 MPa and 250 °C reactor temperature. These findings are very similar to existing literature and thus partially confirm experiment reproducibility. <sup>[2,4]</sup> None of the tested samples show high selectivity towards the reduction of  $CO_2$  to  $CH_4$  (see Figure 7b). The only notable formation of  $CH_4$  is recorded at expected high reactor temperatures for the reference commercial catalyst. 20% CZ, 20% CZC, and 20% CZCZ facilitate minor production of DME, especially the binary 20% CZ catalyst shows selectivity towards MeOH-dehydration to DME with DME-selectivity of 8,6% at 250 °C and 3.5 MPa.

Reaction conditions with the best recorded  $STY_{MeOH}$  and  $CO_2$ -turnover for the coated catalyst in comparison to the reference are given in Table 3.

Best STY<sub>MeOH</sub> results are shown for each catalyst sample with corresponding reactor conditions for the achieved performance. In general, all catalysts expectedly exhibit the highest conversion ratios and production rates at high reactor pressure. Depending on overall catalyst selectivity, maximum production rates are either found at 250 °C or 275 °C reactor temperature. As the conversion rates consistently increase with rising reactor temperatures, the selectivity becomes the defining factor for STY<sub>MeOH</sub>. As can be taken from Figure 7b], CO-selectivity is the defining factor for conversion efficiency as RWGS is the most relevant competing reaction to CO<sub>2</sub>-hydrogenation to MeOH. The generation of CO has wider implications for industrial catalyst deployment. As single pass operation is only applied by a minority of industrial methanol processes, it has to be assumed, that mixed carbon oxide streams will prevail in industrial CO<sub>2</sub>-to-MeOH process applications as CO produced through RWGS is recycled and mixed with CO<sub>2</sub>-based synthesis gas.[2]



Table 3. Conditions with best methanol space time yield (STY) and CO <sub>2</sub> turnover for the coated catalyst in comparison with the reference.						
Catalyst	X <sub>CO2</sub> [%]	STY $[g_{MeOH} g_{Cat}^{-1} h^{-1}]$	GHSV [h <sup>-1</sup> ]	Temp. [°C]	Pres. [MPa]	
Reference	37.8	1.14	12,000	250	5	
20 % CZ	22.2	0.45	10,000	275	5	
20 % CZC	24.2	0.37	12,000	275	5	
20 % CZCZ	16.2	0.51	10,000	250	5	
20 % CZCZC	19.9	0.50	12,000	275	5	

This necessitates more in-depth investigation of catalyst performance for varying carbon-oxide-ratios. Concerning space velocity, no clear conclusions can be made based upon the presented results as depicted in Figure 7b].

All catalysts tend to produce better results in the higher gas hourly velocities for  $10,000\ h^{-1}$  and above.

Finally, the catalyst performance results are also compared to a variety of recent studies that have investigated the same catalyst tuning approaches for more efficient  $X_{CO2}$  and better selectivity for MeOH. In addition, commercial catalysts taken from corresponding patents are also listed for benchmark purposes.

The evaluation criterion was the  $X_{CO2}$  and the  $STY_{MeOH}$ . The results for the study comparison are presented in Table 4. Where available, GSHV, pressure and reactor temperature are added for classification of presented data. If necessary and possible, based upon available study data, GHSV values are converted to  $h^{-1}$  Where different catalyst samples are investigated in the presented studies, maximum values for each sample are used for the comparison presented here.

Most of the catalysts are produced through precipitation, although it is also clear, that impregnation is a viable production method especially for sample catalysts. Seven of the studies use catalyst produced by some form of impregnation. It is notable, that many studies chose GHSV that were considerably lower, than those presented in the study on hand, namely<sup>[11,14,25,26]</sup>. This does not seem to have a negative effect on productivity, which suggests, that GSHV used by the cited commercial applications – from which the herein tested GSHV were adapted - have effects, that could not be replicated in this work. Further testing is needed, for determination of the effects of space velocities in this laboratory work.

Catalyst samples from this work perform very well in comparison to other tested catalysts samples from literature. 20% CZCZ shows the highest STY<sub>MeOH</sub> compared to other selected studies. In part, this can be attributed to the high synthesis pressures used in the test protocols for the presented work in this study. Comparison to other studies, that tested reactor pressures up to 5 MPa still shows, that the catalysts tested herein show superior yield and conversion ratios. The effective surface interplay between ZrO<sub>2</sub> and CeO<sub>2</sub> is thus confirmed. High surface area  $\gamma$ -Al<sub>2</sub>O<sub>3</sub> carrier spheres seem to further boost conversion efficiency. Compared to [32,33] we were able to achieve enhanced STY<sub>MeOH</sub> in this work, proving the potential of the supported catalyst and further highlighting the role of ZnO in the conversion of CO<sub>2</sub> to MeOH.

Concerning metal oxide promoters for  $X_{CO2}$  to methanol,  $ZrO_2$  seems to be widely regarded as the most promising in prolonging active catalyst stability and in delivering active sites for efficient  $CO_2$ -activation. Other additives, that have not been used in production of the catalysts for this study, include Gallium (Ga), Indium (In), Tungsten (W), Nickel (Ni), Platinum (Pt) and Gold (Au). While Ni, In and Pt catalysts supports have shown promising results in converting  $CO_2$  to MeOH, in this application  $Al_2O_3$  proves to be a better choice for large scale utilization due to its wide availability and low price.

# **Conclusions**

A series of infiltration composite catalysts with 20 wt.% active components coating were prepared by IWI method on  $\gamma\text{-Al}_2O_3$  carrier spheres. The catalysts were based on CuO/ZnO and promoted with CeO2, ZrO2 and CaO, which were identified as possible enhancements for the direct hydrogenation of CO2 to MeOH from literature. The IWI method was applied as a simple method for the customized and application-specific production of catalyst samples.  $X_{\text{CO2}}$ , STY $_{\text{MeOH}}$  and selectivity towards MeOH, CO, CH4 and DME were determined in a laboratory test bench at different space velocities, temperatures and pressures and compared to the performance of an industrial Cu-based MeOH catalyst.

Special focus was put on the conversion of  $\text{CO}_2$  to CO and  $\text{H}_2\text{O}$  through RWGS, as it is the main competing reaction in most Cu-based MeOH catalysts.

The binary catalyst complex CuO/ZnO on Al $_2$ O $_3$  carrier spheres reached a maximum conversion rate of 22.2% with STY $_{\text{MeOH}}$  of 0.45  $g_{\text{MeOH}}g_{\text{Cat}}^{-1}h^{-1}$  without additional promotion. The promoted ternary catalyst complex with added CeO $_2$  was not able to improve catalytic performance over 20% CZ. Catalyst promotion toward the quaternary CuO/ZnO/CeO $_2$ /ZrO $_2$  and the quinary CuO/ZnO/CeO $_2$ /ZrO $_2$ /CaO complexes however was able to improve STY $_{\text{MeOH}}$  by 13% and 11% respectively over the binary catalyst formula.

These findings are attributed to extremely high Cu species dispersion on the catalyst. This is supported by the presented XRD, EDX, BET, TPR and TPD results, which suggest an increase in metal species dispersion in the quaternary and quinary catalyst samples and very high surface areas in the supported catalysts. Low ZrO<sub>2</sub>, CeO<sub>2</sub> and CaO loading is confirmed by EDX mappings over SEM images and elemental analysis of the catalyst samples. Formation of multi metal oxide compounds



Recent Advances in Research – CeO <sub>2</sub> , ZrO <sub>2</sub> and alkali metals							
Composition	Sample Manufacturing	GHSV [h <sup>-1</sup> ]	Pressure [MPa]	Temperature [°C]	X <sub>CO2</sub> [%]	$STY_{MeOH} = [g_{MeOH} g_{Cat}^{-1} h^{-1}]$	Ref.
Cu/ZrO <sub>2</sub>	Deposition- Precipitation	10,000	3.00	299	15.80	-	[50]
In <sub>13</sub> /ZrO <sub>2</sub>	Impregnation	12,000	3.00	301	12.50	0.160	[47]
Cu/ZrO <sub>2</sub>	Impregnation Sol-Gel	20,000	3.00	250	1.00	0.144 <sup>[a]</sup>	[19]
Cu-ZnO-ZrO <sub>2</sub>	Precipitation- Reduction	4,600	5.00	263	23.00	0.210	[54]
Cu-ZnO-ZrO <sub>2</sub>	Impregnation Sol-Gel	6,600	3.00	250	19.20	0.376	[14]
CuO-ZnO-ZrO <sub>2</sub>	Reverse Co-Precipitation		2.00	240	14.00	0.219	[18]
CuO-Ga <sub>2</sub> O <sub>3</sub> -ZrO <sub>2</sub>	Impregnation Sol-Gel	20,000	2.00	250	1.16	0.136 <sup>[a]</sup>	[19]
Cu-ZnO-ZrO <sub>2</sub> -Al <sub>2</sub> O <sub>3</sub>	Co-Precipitation	12,000	3.00	250	15.00	0.009	[15]
In <sub>13</sub> /CeO <sub>2</sub>	Impregnation	12,000	3.00	301	0.20	0,008	[47]
Cu/CeO <sub>2</sub>	Deposition- Precipitation	10,000	3.00	300	13.20	-	[50]
CuO/CeO <sub>2</sub>	Hydrothermal	-	3.00	250	-	0.096	[48]
Cu/CeWO <sub>x</sub>	Impregnation	3,000	3.50	250	13.00	0.394	[49]
CuO-ZnO-CeO <sub>2</sub>	Reverse Co-Precipitation	6,000	4.00	260	15.00	0.162	[11]
CuO-ZnO-CeO <sub>2</sub>	Co-Precipitation	4,850 <sup>[b]</sup>	3.00	250	12.30	0.106	[12]
Cu-MgO-Al <sub>2</sub> O <sub>3</sub>	Co-Precipitation	2,000	2.00	200	4.80	_	[25]
CuO-ZnO-Al <sub>2</sub> O <sub>3</sub> -K	Co-Precipitation	2,400	3.00	240	14.00	0.39 <sup>[a]</sup>	[26]
CuO-CeO <sub>2</sub> -ZrO <sub>2</sub>	Gel Co-Precipitation	7,500-24,000 <sup>[b]</sup>	3.00	260	19.00	0.192	[33]
Cu/CeO <sub>2</sub> -ZrO <sub>2</sub>	Co-Precipitation	-	5.00	260	8.00	0.180	[32]
Cu-CeO <sub>2</sub> -ZrO <sub>2</sub>	Co-Precipitation	15,600 <sup>[b]</sup>	5.00	250	3.80	0.076	[55]
Cu-ZnO-ZrO <sub>2</sub> -MgO/Al <sub>2</sub> O <sub>3</sub>	Impregnation	1,500–5,000	2.00	250	12.12	0.031	[24]
This work							
CuO-ZnO-Al <sub>2</sub> O <sub>3</sub>	Co-Precipitation	10,000	5.00	250	38.20	0.840	This Wor
CuO-ZnO/Al <sub>2</sub> O <sub>3</sub>	Impregnation	10,000	5.00	250	10.90	0.199	This Wor
CuO-ZnO-CeO <sub>2</sub> /Al <sub>2</sub> O <sub>3</sub>	Impregnation	10,000	5.00	250	12.30	0.299	This Wo
CuO-ZnO-CeO <sub>2</sub> -ZrO <sub>2</sub> /Al <sub>2</sub> O <sub>3</sub>	Impregnation	10,000	5.00	250	16.20	0.507	This Wo
CuO-ZnO-CeO <sub>2</sub> -ZrO <sub>2</sub> -CaO/Al <sub>2</sub> O <sub>3</sub>	Impregnation	10,000	5.00	250	18.70	0.469	This Wo
Commercial CO-based Methanol C	atalysts						
CuO-ZnO-Al <sub>2</sub> O <sub>3</sub> (Süd Chemie)	Co-Precipitation	10,000	5.00	250	-	1.1	[2, 56]
CuO-ZnO-Al <sub>2</sub> O <sub>3</sub> (BASF)	Co-Precipitation	10,000	5.00	220	-	1.43	[2, 57]
CuO-ZnO-Al <sub>2</sub> O <sub>3</sub> (ICI)	Co-Precipitation	9,600	5.00	230	=	0.43	[2, 58]
Commercial CO <sub>2</sub> -based Methanol C	Catalysts						
CuO-ZnO-Al <sub>2</sub> O <sub>3</sub> -ZrO <sub>2</sub> -SiO (NIRE)	Co-Precipitation	10,000	5.00	250	-	0.76	[2, 59]
[a] Calculated from molar production	on rate. [b] Calculated from r	molar flow rate.					

on the catalyst surface can mostly be ruled out by means of EDX mapping analyses, where ZrO<sub>2</sub> and CeO<sub>2</sub> dispersion over the image mappings is confirmed and the formation of conglomerates of metal oxides cannot be observed. Much rather do the images suggest, that ZrO<sub>2</sub> and CeO<sub>2</sub> express their catalytic qualities through interplay with ZnO and CuO on the

catalyst surface. This is reached while retaining very high surface areas of more than 120  $\text{m}^2\,\text{g}^{-1}$  and similar average pore sizes to the binary carrier catalyst 20% CZ of around  $\text{cm}^3\,\text{g}^{-1}$ .

Total reducibility of the coated catalysts is reduced slightly compared to the commercial catalyst in the tested temperature range. This is expected due to considerably lowered CuO

and-conditions) on Wiley Online Library for rules of use; OA articles are governed by the applicable Creative Comm

loading of the coated catalyst samples. The quaternary catalyst formula exhibits the highest  $H_2$ -consumption of all the tested coated catalyst spheres. This is attributed to the special role of  $ZrO_2$  in providing an effective surface structure for  $H_2$ -adsorption through generation of highly reducible CuO and  $CeO_2$  species on the catalyst surface.

The results show the possible importance in multi metal oxide interplay in inhibiting the desorption of CO in the direct hydrogenation of  $CO_2$ , a key hurdle in developing effective catalysts for the efficient conversion of  $CO_2$  to MeOH. Especially  $ZrO_2$  is herein confirmed as an effective promoter in MeOH synthesis catalysts and its role in interaction with other catalytically active metal oxide components is further underlined. Based upon this work, further testing will be conducted towards the conversion of mixed carbon oxide streams to MeOH. As the main competing reaction to the hydrogenation of  $CO_2$  to MeOH is the formation of CO through RWGS, substantial amounts of CO from previous reactor passes are to be expected in industrial applications with gas recycling, no matter the selectivity of applied catalysts.

This puts special focus on both the selectivity towards carbon conversion to MeOH and the efficiency of the used catalysts in converting both CO and CO<sub>2</sub> to MeOH. Further work will focus on the MeOH production from mixed carbon oxide synthesis gas streams and the mechanics of the competing synthesis paths as a consequence. The effects of recycling the product gas streams will be evaluated in pilot scale application to further study these effects. Furthermore, coated composite catalysts are proven to deliver very good synthesis results in comparison to co-precipitated samples. In addition, the simple preparation method by IWI allows the production of catalyst bodies in a wide range of different geometries with very high catalytic surface areas. Especially spherical catalyst structures are able to optimize catalyst beds regarding homogeneity, heat exchange, feed flow and gas diffusion to the active sites for single tube reactors but also for multi pipe reactors setups and industrial applications of these.

# **Experimental**

#### **Catalyst Preparation**

The infiltration composite catalysts were obtained through impregnation of high surface area aluminum-oxide  $(Al_2O_3)$  spheres with the selected metal oxide mixtures.  $\gamma$ -Al $_2O_3$ -spheres (SASOL, Hamburg Germany) with a nominal diameter of 800  $\mu$ m were used as base for the further production process and loaded with 20 wt% of each catalyst composition, respectively. Water absorption capacity of the carrier was determined through prolonged water bath immersion at 0.64  $q_{H2O}q_{AIOO_3}^{-1}$ .

The highly efficient, proven CuO - ZnO mixture was used as base for all composite samples.<sup>[30]</sup> Molar ratio of CuO and ZnO was set to 2.6:1 for all produced composites, which corresponds to the molar ratio used in the industrial reference catalyst Huton HUC-98 (derived from Süd Chemie Methanol Catalysts<sup>[56]</sup>).

Four carrier catalysts were produced with different molar ratios of added cerium oxide ( $CeO_2$ ), zirconium oxide ( $ZrO_2$ ) and calcium oxide (CaO) using IWI. [63]

Highly water-soluble metal nitrate precursors were used for the catalyst coatings, specifically Cu(NO<sub>3</sub>)<sub>2</sub> \*3 H<sub>2</sub>O (Carl Roth GmbH, Karlsruhe Germany), Zn(NO<sub>3</sub>)<sub>2</sub> \*4 H<sub>2</sub>O (Carl Roth GmbH, Karlsruhe Germany), ZrO(NO<sub>3</sub>)<sub>2</sub> \*2,5 H<sub>2</sub>O (Alfa Aesar GmbH, Kandel Germany), Ce(NO<sub>3</sub>)<sub>3</sub> \*6 H<sub>2</sub>O (Alfa Aesar GmbH, Kandel Germany) and Ca(NO<sub>3</sub>)<sub>2</sub> \*4 H<sub>2</sub>O (Alfa Aesar GmbH, Kandel Germany).

To prepare the infiltration composite spheres with a catalyst content of 20 wt.%, the nitrate salts of the respective metals were first weighed into a beaker according to their molar proportions in the catalyst (Table 5), filled with water to a total volume of 25.6 ml and dissolved by constant stirring.

In each case, 50 g of catalyst spheres with 20 wt.% CuO/ZnO (abbreviated as 20% CZ), CuO/ZnO/CeO $_2$  (abbreviated as 20% CZC), CuO/ZnO/CeO $_2$ /ZrO $_2$  (abbreviated as 20% CZCZ) and CuO/ZnO/CeO $_2$ /ZrO $_2$ /CaO (abbreviated as 20% CZCZC) were obtained. The reference was obtained from industrial 6 mm catalyst pellets by crushing and sieving to a fraction between 800–900  $\mu$ m diameter for comparability and reactor occupancy similar to the produced carrier catalyst samples.

#### **Sample Characterization**

Analyses of specific Brunauer-Emmett-Teller (BET) surface areas, pore size distribution and pore volume were carried out on an automated surface area analyzer (Micromeritics ASAP 2060) for each presented catalyst sample. Samples were tested for  $N_2$ -adsorption and desorption isotherms at  $-196\,^{\circ}$ C. For pretreatment,

Table 5. Molar composition of the catalyst fractions within the infiltration composites.							
Sample	CuO cont.mol-%	ZnO-cont. mol-%	CeO <sub>2</sub> -cont. %mol	ZrO <sub>2</sub> -cont. %mol	CaO-cont. %mol		
CuO/ZnO <sup>[a]</sup> (20% CZ)	72.2	27.8	-	-	-		
CuO/ZnO/CeO <sub>2</sub> <sup>[a]</sup> (20% CZC)	65	25	10	-	-		
CuO/ZnO/CeO <sub>2</sub> /ZrO <sub>2</sub> <sup>[a]</sup> (20% CZCZ)	57.8	22.2	10	10	-		
CuO/ZnO/CeO <sub>2</sub> /ZrO <sub>2</sub> /CaO <sup>[a]</sup> (20% CZCZC)	54.2	20.8	10	10	5		
[a] As coating for 20 wt% on $\gamma$ -Al <sub>2</sub> O <sub>3</sub> -spheres (800 $\mu$ m).							

samples were evacuated for 2 h at room temperature. The resulting adsorption isotherms are plotted in the supplementary materials to this manuscript.

XRD was performed using Empyrean (Malvern Panalytical B.V., Netherlands) with CuK $\alpha$  radiation at 45 kV and 40 mA. XRD data were collected in a Bragg-Brentano geometry in the  $2\Theta$  range of  $10^\circ-90^\circ$  with  $\triangle 2\Theta$  of  $0.026^\circ$  and a counting time of 250 s/step using a 255-channel PIXcel linear detector.

For topographic analysis of the sample surfaces, scanning electron microscopy (SEM) images were taken of the catalyst surfaces using a JEOL JSM-IT800 microscopy unit. Additionally, Energy Dispersive X-ray Spectroscopy (EDX) was conducted in-situ using an EDAX Octane Elect Super system (70 mm² chip). SEM- and EDX-analyses were conducted at room temperature, samples were loaded unreduced.

For determination of catalyst redox properties,  $H_2$ -TPR of the samples was conducted. Experiments were carried out at ambient pressure on the automated Micromeritics 2950 MicroActive. For each TPR-measurement run, typically about 100 mg of every catalyst sample was tested in an auto flow quartz reactor. Samples were pretreated in-situ at 200 °C for 30 minutes in helium. Afterwards, reduction was conducted with 5 %  $H_2$  in Argon at 10 °C/min from 35 °C to 600 °C. Measurements of consumed  $H_2$  were carried out using a TCD detector.

For specification of catalyst surface acid sites, NH<sub>3</sub>-TPD was performed for every catalyst sample on the same device.

Catalyst preparation was carried out according to the aforementioned preparation and pretreatment protocol. The catalyst samples were treated with 10% NH<sub>3</sub> in helium carrier gas until the quartz reactor effluent TCD measurement returned to stable baseline indicating full adsorption of ammonia to the different surface acid sites. Samples were flushed with helium from 50°C to 500°C at a

heating rate of  $10\,^{\circ}\text{C}$  per minute. Desorbed ammonia was measured using TCD of the reactor outlet.

#### **Catalyst Performance**

Catalyst performance was determined using a laboratory test bench (Figure 8) equipped with a single tubular reactor with 70 ml dedicated catalyst volume and 25 mm inner diameter.

All gases were supplied through high pressure cylinders. Gas dosing and control of total volume flow were implemented by high pressure bandwidth mass flow controllers (Bronkhorst El-Flow C200 Series for CO and  $H_2$  and Bronkhorst mini CORI-Flow for  $CO_2$ ).

Reactor pressure was controlled through a proportional flow valve and a pressure control valve at the end of the total pressurized gas section and pressure regulators for each gas dosing section. Reactor temperature was controlled in counter flow configuration using a thermo-oil-cryostat. Product gas composition at reactor outlet was determined by an online gas chromatography unit (Shimadzu GC2030 AT) with column – Rt-U-Bond Plot, 30 m×0.53 mm – and mol sieve SH MSieve 5 A–30 m×0.53 mm – in serial configuration and TCD. Helium was used as carrier gas.

The liquid samples were collected in a high-pressure flash after condensation in a cooling section and drawn into containers through a solenoid back pressure valve.

Liquid samples were additionally analysed for their composition and by-product contents ex-situ on a HPLC unit (Shimadzu LCMS-2020).

Finally, dry off-gas was expanded and total dry gas mass flow rate was measured. Off-gas composition was determined using inline CO<sub>2</sub>- and H<sub>2</sub>-measurements (BlueSense BCP-CO<sub>2</sub> and BCP-H<sub>2</sub>) and an online unit for additional redundant measurement of CO<sub>2</sub>- and CO-content (Emerson NGA2000).

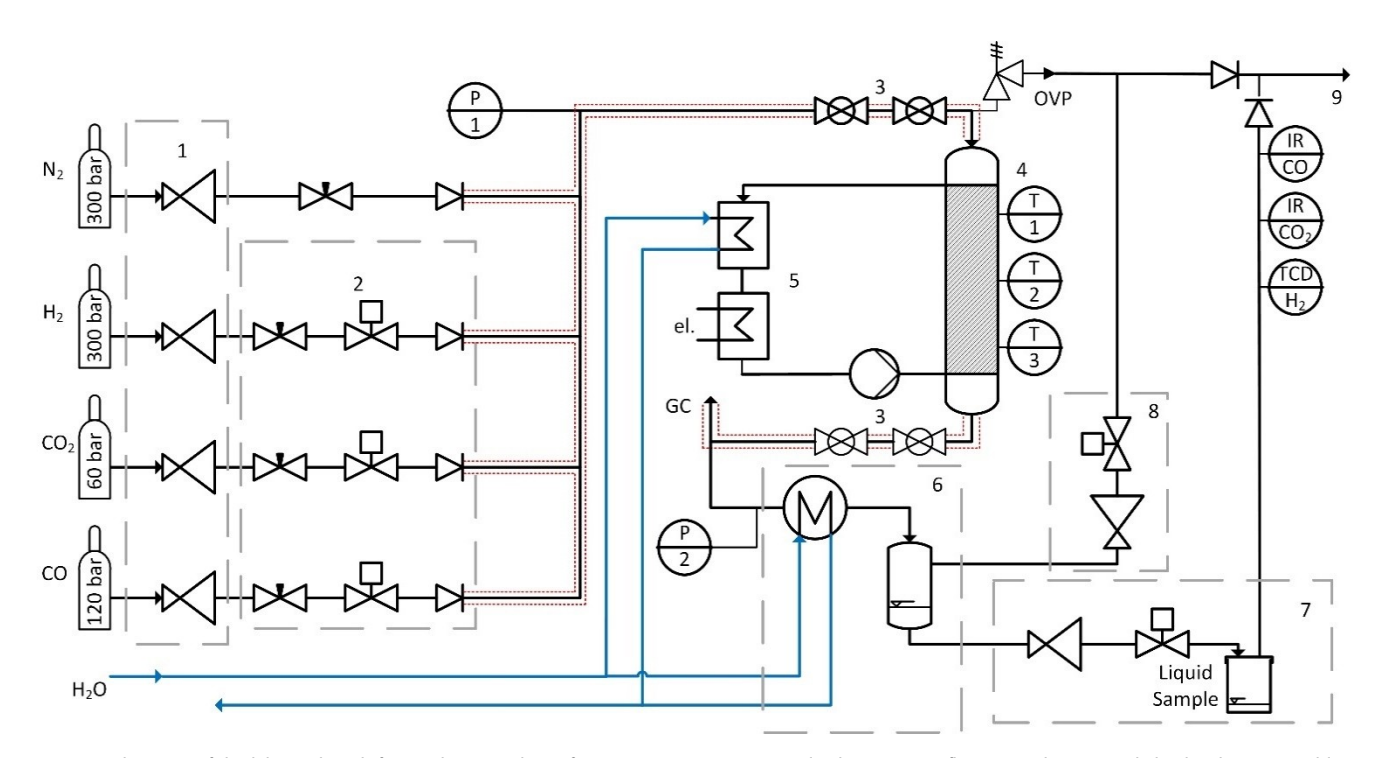


Figure 8. Schematic of the lab test bench for catalyst sample performance. 1: Pressure control valves; 2: Mass flow control (MFC) and check valves; 3: Double valve coupling for reactor removal; 4: Reactor with three temperature measurements; 5: Electro-thermal oil heating/cooling; 6: Product cooling and flash; 7: Liquid sample; 8: Flow control and expansion valve; 9: Exhaust.

For testing catalyst performance, 70 ml of each sample were gauged by volume and then weighed. Catalyst was filled into the reactor and excess volume was topped with quartz wool as filling agent and additional gas dispersion.

Each catalyst sample was reduced in 100%  $\rm H_2$  flow. For reduction, reactor temperature was programmed from 50 °C to 300 °C in 10 °C increments every 10 min.

Molar flow rates and mass flow rates for the reactor exit gas were determined by assuming conservation of mass from dosed gases and calculating product gas molar weight. Total mass flow rates  $(m_{TOT})$  were calculated by summing dosed masses from MFCs through Equation (5), product gas mixture molar mass was determined through Equation (6)  $(M_{Product})$ . Total product flow rate was calculated through Equation (7)  $(n_{Product})$ :

$$\dot{m}_{TOT} = m_{CO_2} + m_{H_2} + m_{CO}$$
 (5)

$$M_{Product} = \sum_{1}^{n} y_{product,i} \cdot M_{i}$$
 (6)

$$\dot{n}_{Product} = \frac{\dot{m}_{TOT}}{M_{Product}} \tag{7}$$

y<sub>Product</sub>, was derived from GC measurement of product gas molar composition. Each experiment was carried out once with 5 key experiments per catalyst sample being repeated threefold for demonstration of repeatability.

# **Supporting Information**

Supporting information for  $N_2$ -physisorption tests and EDX-analyses is added in supplementary materials document. Further supporting information and project Data are available on reasonable request from the corresponding author.

# Acknowledgements

This work was supported by the German Ministry of Economic Affairs and Climate Action through the Inno-Kom program (GREEN-BEE, 49VF190052) and general funding from federal budget (Methanolstandard, 19I20005D). Furthermore, the research was supported by direct funding by MVA Müllverwertungsanlage Bonn GmbH. We would like to thank Noah Avraham-Radermacher of the Institute of Technical and Macromolecular Chemistry (ITMC) in Aachen and for their support in physio-chemical analysis of the catalyst samples. The authors gratefully acknowledge Dr. You Jung Sohn from IEK-1 for performing the XRD investigations. Open Access funding enabled and organized by Projekt DEAL.

# **Conflict of Interests**

The authors declare no conflict of interest.

# **Data Availability Statement**

The data that support the findings of this study are available from the corresponding author upon reasonable request.

**Keywords:** methanol synthesis · RWGS · incipient wetness impregnation method · CO<sub>2</sub> hydrogenation

- [1] G. Liu, H. Hagelin-Weaver, B. Welt, Waste. 2023, 1(1), 228-248.
- [2] V. Dieterich, A. Buttler, A. Hanel, H. Spliethoff, S. Fendt, Energy Environ. Sci. 2020, 13, 3207–3252.
- [3] F. ARENA, K. Berbera, G. Itlaliano, G. BONURA, L. SPADARO, F. Fursteri, J. Catal. 2007, 249(2), 185–194.
- [4] H. Ruland, H. Song, D. Laudenschleger, S. Stürmer, S. Schmidt, J. He, K. Kähler, M. Muhler, R. Schlögl, ChemCatChem 2020, 12(12), 3216–3222.
- [5] U. J. Etim, Y. Song, Z. Zhong, Front. Energy Res. 2020 8 (8), 545431.
- [6] M. Ren, Y. Zhang, X. Wang, H. Qiu, Catalysts. 2022, 12(4), 403.
- [7] C. S. Santana, L. F. Rasteiro, F. C. Marcos, E. M. Assaf, J. F. Gomes, J. M. Assaf, Molecular Catalysis. 2022, 528, 112512.
- [8] P. Sharma, J. Sebastian, S. Ghosh, D. Creaser, L. Olsson, *Catal. Sci. Technol.* 2021, 11(5), 1665–1697.
- [9] X. Hu, W. Qin, Q. Guan, W. Li, ChemCatChem 2018, 10(19), 4438-4449.
- [10] F. Jiang, S. Wang, B. Liu, J. Liu, L. Wang, Y. Xiao, Y. Xu, X. Liu, ACS Catal. 2020, 10(19), 11493–11509.
- [11] Z. Luo, J. Guo, G. T. Hu, Z. Wang, Greenhouse Gases Sci. Technol. 2021, 11, 171–1179.
- [12] R. Singh, K. Kundu, K. K. Pant, Chem. Eng. J. 2024, 479, 147783.
- [13] M. Nie, A. Cui, M. Wu, T. Guo, Q. Guo, J. CO<sub>2</sub> Util. 2023, 75, 102579.
- [14] M. Mureddo, F. Ferrara, A. Pettinau, Appl. Catal., B 2019, 258, 117941.
- [15] H. Jeong, C. H. CHo, T. H. Kim, React. Kinet., Mech. Catal. 2012, 106, 435–443.
- [16] K. Larmier, W.-C. Liao, S. Tada, E. Lam, R. Verel, A. Bansode, A. Urakawa, A. Comas-Vives, C. Copéret, Angewandte Chemie (International ed. in English). 2017, 56(9), 2318–2323.
- [17] J. Yu, S. Liu, X. Mu, G. Yang, X. Luo, E. Lester, T. Wu, Chem. Eng. J. 2021, 419, 129656.
- [18] T. Witoon, N. Kachaban, W. Donphai, P. Kidkhunthod, K. Faungnawakij, M. Chareonpanich, J. Limtrakul, Energy Convers. Manage. 2016, 118, 21– 31.
- [19] E. L. Fornero, P. B. Sanguineti, D. L. Chiavassa, A. L. Bonivardi, M. A. Baltanás, Catal. Today 2013, 213, 163–170.
- [20] X. Mao, Y. Zhang, Y. Xu, Y. Zhou, K. Zhuang, K. Shen, S. Ding, Catal. Sci. Technol. 2024, 14(2), 419–430.
- [21] K. Stangeland, H. H. Navarro, H. L. Huynh, W. M. Tucho, Z. Yu, Chem. Eng. Sci. 2021, 238, 116603.
- [22] A. Bansode, B. Tidona, P. R. von Rohr, A. Urakawa, Catal. Sci. Technol. 2013, 3(3), 767–778.
- [23] P. Kowalik, W. Próchniak, T. Borowiecki, Catal. Today 2011, 176(1), 144– 148.
- [24] H. Ren, C.-H. Xu, Hao Zhao, Y.-X. Yang, Wang, J. Liu, J.-Y. Liu, J. Ind. Eng. Chem. 2015, 28, 261–267.
- [25] V. D. Dasireddy, N. S. Stefanci, B. Likozar, J. CO<sub>2</sub> Util. 2018, 28, 189–199.
- [26] N. Pasupulety, A. A. Al-Zahrani, M. A. Daous, S. Podila, H. Driss, *Arabian J. Chem.* 2021, 14(2), 102951.
- [27] K. Xiao, Q. Wang, L. Zhong, Catal. Lett. 2017, 147, 1581–1591.
- [28] F. Studt, M. Behrens, E. L. Kunkes, N. Thomas, S. Zander, A. Tarasov, J. Schumann, E. Frei, J. B. Varley, F. Abild-Pedersen, J. K. Nørskov, R. Schlögl, ChemCatChem 2015, 7(7), 1105–1111.
- [29] I. Orozco, E. Huang, M. Mahapatra, J. Kang, R. Shi, S. Nemšák, X. Tong, S. D. Senanayake, P. Liu, J. A. Rodríguez, J. Phys. Chem. C. 2021, 125(12), 6673–6683.
- [30] M. Zabilskiy, V. Sushkevic, D. Palagin, M. Newton, F. Krumeich, J. Wang, Nat Commun. 2020, 11, 2409.
- [31] D. Kordus, J. Jelic, M. Lopez Luna, N. J. Divins, J. Timoshenko, S. W. Chee, C. Rettenmaier, J. Kröhnert, S. Kühl, A. Trunschke, R. Schlögl, F. Studt, B. Roldan Cuenya, J. Am. Chem. Soc. 2023, 145(5), 3016–3030.
- [32] M. Zabilskiy, K. Ma, A. Beck, J. van Bokhoven, Catal. Sci. Technol. 2021, 11, 349–358.
- [33] S. Poto, D. van Berkel, F. Gellucci, F. d'Angelo, Chem. Eng. J. 2022, 435, 134946.
- [34] L. Yao, X. Shen, Y. Pan, Z. Peng, J. Catal. 2019, 372, 74–85.



- [35] T. Phongamwong, U. Chantaprasertporn, T. Witoon, T. Numpilai, Y. Pooarporn, W. Limphirat, W. Donphai, P. Dittanet, M. Chareonpanich, J. Limtrakul, Chem. Eng. J. 2017, 316, 692–703.
- [36] G. Bonura, F. Arena, G. Mezzatesta, C. Cannilla, L. Spadaro, F. Frusteri, Catal. Today 2011, 171(1), 251–256.
- [37] Z. Shi, Q. Tan, D. Wu, Mater. Chem. Phys. 2018, 219, 263–272.
- [38] T. P. Mabate, N. P. Maqunga, S. Ntshibongo, M. Maumela, N. Bingwa, SN Appl. Sci. 2023, 5, 7.
- [39] C. Haung, S. Chen, X. Fei, D. Liu, Y. Zhang, Catalysts. 2015, 5, 1846-1861.
- [40] J. C. Slaa, J. G. van Ommen, J. Ross, Catal. Today 1992, 15(1), 129-148.
- [41] P. Forzatti, E. Tronconi, I. Pasquon, *Catal. Rev.* **1991**, 33(1–2), 109–168.
- [42] E. Yang, E. J. Jang, J. G. Lee, S. Yoon, J. Lee, N. Musselwhite, G. A. Somorjai, J. H. Kwak, K. An, Catal. Sci. Technol. 2018, 8(13), 3295–3303.
- [43] H. Pines, W. O. Haag, J. Am. Chem. Soc. 1960, 82(10), 2471–2483.
- [44] M. Gnanamani, R. Garcia, G. Jacobs, K. Gora-Marek, D. Cronauer, J. Kropf, C. Marshall, M. K. Gnanamani, K. Góra-Marek, D. C. Cronauer, A. J. Kropf, C. L. Marshall, *Appl. Catal.*, A 2020, 602, 117722.
- [45] T. Viinikainen, H. Rönkkönen, H. Bradshaw, H. Stephenson, S. Airaksinen, M. Reinikainen, P. Simell, O. Krause, Appl. Catal., A 2009, 362(1–2), 169– 177.
- [46] K. Tanabe, Mater. Chem. Phys. 1985, 13(3-4), 347-364.
- [47] P. Sharma, P. Hoang Ho, J. Shao, D. Creaser, L. Olsson, Fuel. 2023, 331, 125878.
- [48] J. Zhu, Y. Su, J. Chai, V. Muravev, N. Kosinov, Hensen, Emiel, ACS Catal. 2020, 10, 11532–11544.
- [49] Y. Yan, R. J. Wong, Z. Ma, F. Donat, S. Xi, S. Saqline, Q. Fan, Y. Du, A. Borgna, Q. He, C. Müller, W. Chen, A. Lapkin, Appl. Catal., B 2022, 306, 121098.
- [50] W. Wang, Z. Qu, L. Song, Q. Fu, *J. Energy Chem.* **2020**, *40*, 22–30.

- [51] W. Liao, W. Liao, P. Liu, ACS Catal. 2020, 10(10), 5723-5733.
- [52] N. Azhari, D. Erika, St. Mardinia, T. Ilmi, M. Gunawan, I. Makerthihartha, Results Eng. 2016, 16, 100711.
- [53] S. G. Jadhav, P. D. Vaidya, B. M. Bhanage, J. B. Joshi, Chem. Eng. Res. Des. 2014, 92(11), 2557–2567.
- [54] X. Dong, F. Li, N. Zhao, F. Xiao, J. Wang, Y. Tan, Appl. Catal., B 2016, 191, 8–17.
- [55] Y. Attada, V. K. Velisoju, H. O. Mohamed, A. Ramirez, P. Castaño, J. CO<sub>2</sub> Util. 2022, 65, 102251.
- [56] M. Schneider, K. Kochloefl, J Ladebeck, EP0125689A2. 1984.
- [57] F. Bröcker, K.-H. Gründler, M. Lazslo, M. Schwarzmann, B Triebskorn, US4436833A. 1984.
- [58] J. Gallagher, J. Kidd, GB1159035A. 1966.
- [59] T. Masami, M. Hirotaka, W. Taiki, U. Michiaki, M. Takashi, M. Kozo, K. Uchikoshi, US6048820 A. 1998.
- [60] O. Martin, C. Mondelli, D. Curulla-Ferré, C. Drouilly, R. Hauert, J. Pérez-Ramírez, ACS Catal. 2015, 5(9), 5607–5616.
- [61] K. Sun, N. Rui, Z. Zhang, Z. Sun, Q. Ge, C.-J. Liu, Green Chem. 2020, 22(15), 5059–5066.
- [62] N. K. Zimmerli, L. Rochlitz, S. Checchia, C. R. Müller, C. Copéret, P. M. Abdala, JACS Au. 2024, 4(1), 237–252.
- [63] K. de Jong, Synthesis of Solid Catalysts, Wiley VCH, Hoboken 2009.

Manuscript received: April 19, 2024 Revised manuscript received: July 8, 2024 Accepted manuscript online: July 14, 2024 Version of record online: September 6, 2024